ORIGINAL PAPER

On the Influence of Sampling Scale on the In Situ Block Size Distribution

Maurizio Bernardini[1] · Carlos Paredes[1] · José A. Sanchidrián[1] · Pablo Segarra[1] · Santiago Gómez[1]

Abstract

The modelling of discontinuities in rock mass is undertaken with different measurement techniques and used to determine the in situ block size distribution (IBSD). Two monitoring techniques are employed: televiewer logging of boreholes and photogrammetry of highwall faces in a quarry bench; televiewer performs at the borehole diameter scale, while photogrammetry surveys at the entire bench scale. Ground sampling distances were, respectively, about 1 and 8.5 mm. The discontinuities are modelled as a stochastic discrete fracture network (DFN), with the number of discontinuities used in the simulation calibrated by the intensity per unit length (P_{10}) on the televiewer data, or by the fracture density (P_{21}) on the photogrammetry data, leading to different fracture networks. From the discontinuity network models, the IBSDs are calculated and discussed as function of the sampling scale (i.e. televiewer or photogrammetry data source) and of the fracture density. The goal is to compare the results from both techniques for rock mass structural characterization, to assess their limitations and shortcomings, and to show their potential complementarity at different sampling scales. The televiewer data provides smaller block sizes than the photogrammetry, following the higher number of fractures observed in the former. All volumetric distributions obtained are extremely well represented by Gamma with a power law tail distribution. Despite different location parameters, it is particularly remarkable that all distributions present very similar Gamma shape parameters. The constant log–log slopes of the tails provide evidence of multi-scale validity and a scaling invariant structure (more than two orders of magnitude) of discontinuities of the rock mass. The IBSDs and the scale effect are discussed in the light of the fragment size distributions from blasts carried out in the area characterized.

Highlights

- Optical televiewer logs and photogrammetrical models are used to determine the discontinuity maps and the In-Situ Block Size Distribution (IBSD)
- The differences of the discontinuity distributions from both measurement techniques, and the resulting discrete fracture networks, are discussed
- Televiewer data provide smaller block sizes than the photogrammetry ones. This seems to be related with the smaller ground sampling distance of televiewer

- Gamma distribution shape parameters for all IBSD, i.e. log-log slopes of the IBSD, are nearly constant for all distributions, despite their different sizes
- The IBSD are discussed in view of the fragment size distributions from blasts conducted in the block characterized

✉ José A. Sanchidrián
ja.sanchidrian@upm.es

1 Universidad Politécnica de Madrid – ETSI Minas y Energía, Ríos Rosas 21, 28003 Madrid, Spain

🙋 Springer

1 Introduction

The discrete fracture network (DFN) modelling is an effective tool to obtain a high-quality characterization of the rock mass (Dershowitz and Einstein 1988; Dershowitz et al. 2004; Miyoshi et al. 2018; Elmo et al. 2021). For that, fracturing information must be obtained at an arbitrarily selected scale. The choice of this scale is subject to principles of economy, geographical accessibility, resources or database availability. Commonly chosen scales range from fracture-plane information obtained from morphostructural lineaments and geological mapping from the exposure of natural or man-made rock outcrops, to larger-scale fracture-hosting geological structures, or major discontinuities interpreted from, e.g. site geophysical surveys (Kattenhorn and Pollard 2001; Boersma et al. 2020).

The discontinuity mapping may be done in practice by on-site inspection of exposed rock surfaces, such as natural outcrops or, in a mining environment, bench highwalls. The scanline is the classical method by which lines are drawn on the outcrop surface, and orientation and dip angles of all joints intersecting the line are measured. In a mine or quarry, scanlines can be conveniently performed on the highwalls. Semi-automatic extraction of rock mass structural data from high-resolution LiDAR point clouds, or from photogrammetry models (Riquelme et al. 2014), has brought a significant advance to the knowledge of the rock mass in mining, be it in safety or in production applications. Such models of the bench faces are available nowadays from inexpensive equipment and processing software, and most mine design and modelling tools incorporate the capacity of importing such digital models.

Lu (1997) compared the in situ and the post-blast size distribution to analyse the blastability of the rock mass. Brzovic et al. (2015) demonstrated that the 3D volumetric fracture density (P32) controls the overall fragmentation of the rock mass in block caving. Wang et al. (2003) developed a software to analyse the characteristics of discontinuities in an ore body and predict the size distribution of ore fragments in block caving. Medinac et al. (2018) applied UAV technology to assess the pre- and post-blast rock fragment size distribution, as well as blast performance. Elmouttie and Poropat (2012) showed that fragmentation prediction can be made from IBSD of jointed mass with relatively small discontinuities. Junkin et al. (2019) used a rock engineering system (RES) approach to generate a fragmentation interaction matrix of controllable parameters, i.e., blast design, explosive energy and blast timing, and uncontrollable parameters, i.e. the physical and structural properties of the intact rock. Aler et al. (1996) compared the in situ block size distribution with the fragment size distribution of the corresponding muck

after blasting and assessed the predominant influence of the initial structure of the rock mass on the subsequent blasting results. Latham et al. (2006) present a practical step-by-step methodology for IBSD assessment. Work initiated by White (1977) and extensively developed by Stavropoulou (2014) derived a closed-form solution that could be used to predict the IBSD in a rock mass containing three sets of joints with different spacings, based on the fracture frequency of the rock mass. However, in tectonically complex zones, it is common to find more than three fracture families, so the IBSD cannot be defined using the principal mean spacing (Latham and Lu 1999).

The present work gives an insight into the use of photogrammetry models for fracture measurement, the results of which are compared with structural data obtained from borehole image scanning. The two methods are carried out in pairs to complement the database and compensate intrinsic sampling biases due to the limitations of each technique that are used to obtain complete 3D synthetic fracture networks. Photogrammetry acquisition presents some limitations such as a lower-resolution and a time-consuming mapping phase. Besides, the quality of the photos (mainly sharpness and contrast) may compromise the significance of the resulting tracemaps. On the other hand, televiewer logging implies a high-cost technology, the acquisition is also time-consuming and presents difficulties in detecting fractures near-parallel to the borehole. The presence of dust or mud on the borehole walls could affect the reconstruction of the virtual core. Finally, both techniques require the training of the operator who performs the acquisition and post-processing phases.

Photogrammetry models of highwall faces were analysed for visible joint traces by ShapeMetriX 3D® and BlastMetriX 3D® softwares (3GSM 2010a, b). Besides, scanning of the inner surface of boreholes was made by an optical televiewer and discontinuities observed and measured by the WellCAD® software (Advanced Logic Technology 2017). From the orientation and position of the discontinuities measured by the televiewer, and from the orientation and maps of traces measured on the photogrammetry models, discrete fracture network (DFN) models are generated using the FracMan® suite (Golder Associates Inc 2018). From them, the distributions of volumes of the blocks formed from the fractures' intersections (the in situ block size distribution, IBSD) are derived. The different sampling scales and sampling characteristics associated to both monitoring techniques involve a different baseline information on the discontinuities structure that encompasses fracture networks with different characteristics, ultimately resulting in apparently different IBSDs. Such differences, but also some relevant similarities, are highlighted and discussed.

2 Data Collection

The test site is El Aljibe, a quarry located in Almonacid de Toledo, Spain, that mines mylonites and other metamorphic rocks used as aggregates for track ballast, mainly for high-speed and conventional railway construction. The open pit is located within the Toledo Shear Zone that separates two discrete structural and metamorphic units of the Central Iberian massif: the Toledo Migmatite Complex unit to

the north, and the Paleozoic metasediments intruded by the Orgaz granodiorite to the south (Enrile 1991). Three tectonic phases of Hercynian syn-metamorphic structure are observed in both the Migmatites Complex and the Palaeozoic metasediments, with folds tending NW–SE, E–W and N–S, respectively (Enrile 1991).

The highwall faces and boreholes of the blasts that were used for the fractures mapping were located in two blocks on the lower level of the pit, on its southwestern edge (Fig. 1,

Fig. 1 Study area in the lower bench of the pit. The dashed line on the upper bench face marks the trace of a fault
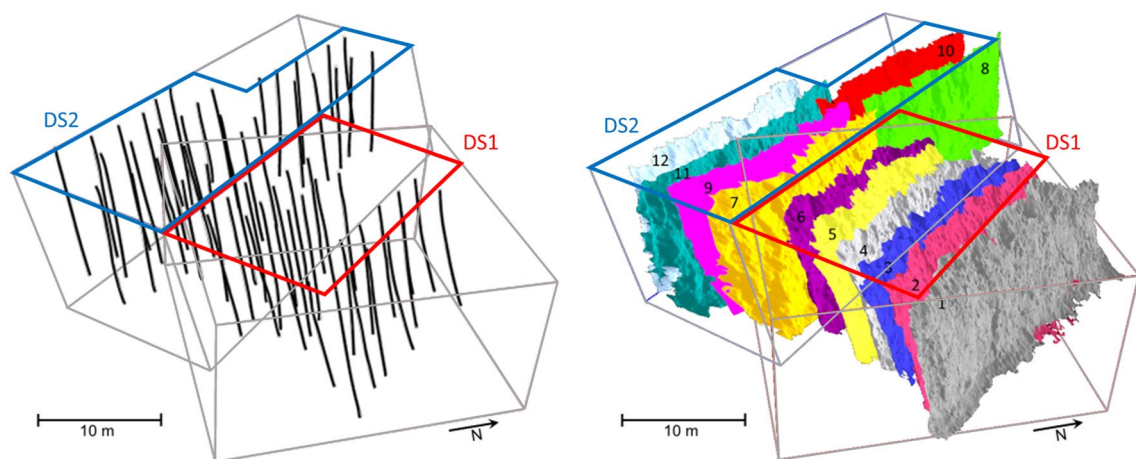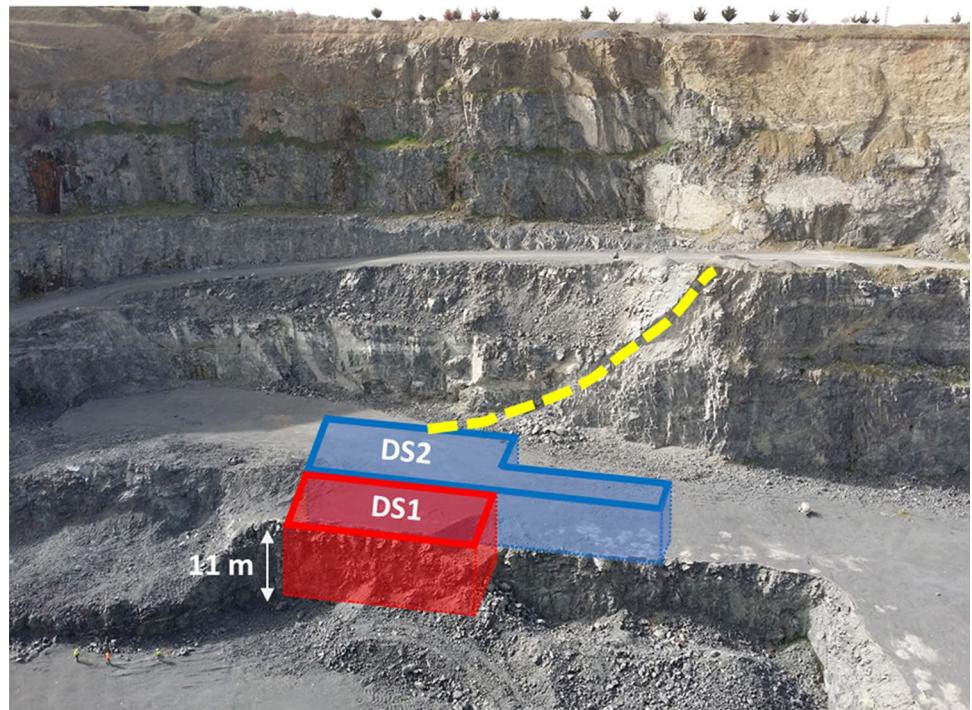

Fig. 2 Fifty-seven boreholes (left) and 12 highwall models (right) for DS1 (red) and DS2 (blue). The thin grey lines define the volumes considered for the stochastic simulation of the DFN models ('region boxes', see "Discrete Fracture Network Models and In Situ Block Size Distributions") (Color figure online)

marked DS1 and DS2). The two blocks were excavated in two separate blasting campaigns. Once the joint maps were analysed, it appeared that there was a potential difference in the structural characteristics of the two blocks, likely due to the influence of a major fault, see "Fracture Domains and Discontinuity Sets". Fracture data were collected from optical televiewer scans of the inner surface of 57 boreholes, and from photogrammetry models of the highwall faces of 12 blasts. The location of the boreholes and the highwalls is shown in Fig. 2.

Photogrammetry inspects the fractures outcropping the highwall surface, while televiewer investigates fractures that intersect the boreholes. The observation distance is some tens of metres for photogrammetry and some centimetres for optical televiewer, hence the ground sampling distance (the size on the ground of an image pixel, GSD) is greater with photogrammetry than with televiewer, even if the pixel array is denser in the photogrammetry. GSD, image quality (contrast and brightness, mainly), the capacity of the human eye, the expert skills of the operator and the capacity of the automatic recognition system influence the sampling scale (i.e. the minimum size of a morpholine that can be detected, based on an aligned sequence of pixels in the image). In our case, the sampling scales are about 10^{-2} m for photogrammetry and 10^{-3} m for televiewer, on average. This means that traces (i.e. an aligned recognized sequence of pixels) observed in the borehole logs may not be observable in the photogrammetric models of the highwalls.

Additional data on the orientation of discontinuities was also collected by structural sampling outside the quarry, to establish the relationship with the structural geological setting and to help adjust the distribution functions of the orientations of the families. Three outcrops of small dimensions (around 10–20 m^2) were found, located on a nearby hill about 1100–1300 m west of the quarry. Among the different strategies used for outcrop sampling of the fracture orientations (Priest 1983; Rohrbaugh et al. 2002; Zhang et al. 2021), a variation of the area method (Wu and Pollard 1995) was selected and adapted to the outcrop geometry. The outcrops that constitute structural measuring stations had faces with different orientations and aspects, which reduced the possible bias in the orientation of the fractures. After visual inspection and recognition of each structural mode of the area (Enrile 1991), more than 20 orientation data were taken with a compass (Zhang et al. 2021) along the entire length of the outcrop.

Orientations (dip directions and dips) were taken at: (i) several points on the same discontinuity and (ii) different discontinuity planes for each identified mode, depending on the quality of the outcrop planes (clarity in the definition of the plane to be measured), so as to assess the dispersion around the sampled mode. A total of 167 structural measurements were taken that allowed to sample surfaces with orientation different from the highwalls and the boreholes, providing complementary information which helped compensate the relative orientation sampling bias of the televiewer and photogrammetry fracture data.

2.1 Televiewer Probe

The number of boreholes surveyed with optical televiewer and the total length investigated are given in Table 1. Only the bench face was monitored in blast B3. An ALT device was used, composed of a QL40 OBI-2G logging tool with a hole orientation system and a digital image sensor at the bottom, with an active pixel array of 1.2 Mpx and fisheye matching optics. The azimuthal resolution was 0.3 mm/px and the vertical resolution 1 mm/px.
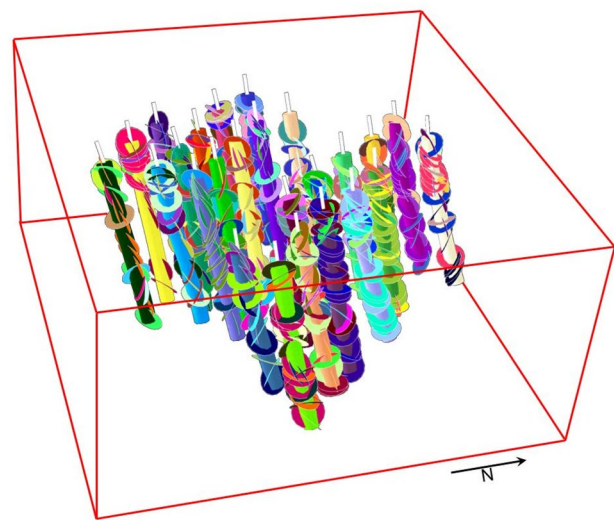

Fig. 3 Distribution of the fractures mapped along each borehole of the DS1 campaign by means of optical televiewer; fractures are arbitrarily represented as circles of 1 m

Table 1 Number, length of boreholes, and number of fractures monitored with televiewer for each blast

Blasts	B1	B2	B3	B4	B5	B6	B7	B8	B9	B10	B11	B12
No. of boreholes	6	6	–	5	5	3	5	5	5	5	6	6
Total length of holes, m	71.8	64.8	–	61.1	60.4	36.4	55.9	59.6	48.2	48.4	62.0	70.2
No. of located fractures	170	138	–	114	117	58	231	237	216	254	242	364

The televiewer provides a continuous unwrapped, oriented coloured cylinder of the hole wall for each borehole. The visual mapping of the in-hole image logs was performed using WellCAD® software. Post-processing determines the position (depth) of the intersection of the discontinuities with the borehole, as well as their orientations. The small diameter of the borehole severely limits any information on the discontinuity size (persistence), shape, or termination behaviour (Brown 2002; Kaiser et al. 2015). Some examples of the televiewer-measured fractures are shown in Fig. 3.

2.2 Photogrammetry Scan

Terrestrial close-range photogrammetry was performed to produce 3D synthetic models of the bench faces from two to three pairs of stereographic photos made 30–35 m from the highwall. A Canon EOS70D digital camera with a sensor of 20 Mpx equipped with a Tamron 17–50 mm optical lens was used for the acquisition. The focal distance, the highwall height and the sensor dimension resulted in an average GSD of 7.3–8.5 mm/px. To scale, orient and locate the synthetically reconstructed 3D model, six to eight disk targets were distributed on the face of the bench block as ground control georeferenced points (red dots in Fig. 4). The area and orientation of the highwall surfaces surveyed are given in Table 2.

BlastMetriX 3D® software was used for creating the 3D synthetic and oriented surfaces, on which the discontinuity trace recognition was made with the aid of ShapeMetriX 3D® software by the same operator that inspected the televiewer logs. The operator fits a polyline or a polygon to traces and surfaces, respectively ,observed in the model; see Figs. 5 and 6. The software fits a plane to the point cloud to calculate the orientation (dip direction and dip angle) of each discontinuity. The mapping of highwall faces and outcrops provides a wider observation window than inside boreholes, enabling the investigation of the size of the fractures and their spatial co-relationships, in addition to fracture spacing. The number and length of the marked traces are shown in Table 2.

2.3 Fracture Domains and Discontinuity Sets

Figure 7 shows cumulative fracture intensity plots in the vertical direction for some sample boreholes corresponding to blasts in different blocks of the area studied, evidencing vertical structural homogeneity. According to regional tectonic information, there is a major normal fault that strikes NW–SE approximately 100 m from the monitored area. A parallel fault was recognized, probably belonging to the secondary fracturing damage zone associated with an accommodation process after the main faulting stress release, crossing the south side of the free face of blasts B11 and B12 (see Fig. 1). Its dip direction and dip angle are 210° and 84°, respectively. To assess the influence of this structure in our data, the fracture intensity, i.e. number of fractures divided by the inspected hole length with televiewer, is plotted versus the minimum distance of the hole to the fault; see Fig. 8. The total fracture intensity decreases significantly with the distance to the fault, and the influence zone seems to reach about 12–15 m. From the plot, the data can be classified into two structural domains which roughly correspond to the blocks of the two blast campaigns—the two datasets are also named hereafter DS1 and DS2. A low fracture intensity of about 2 m^{-1} with a limited dispersion is observed in dataset DS1 (blasts B1 to B6, cross markers), while a higher intensity of about 4 m^{-1} with a higher variability is observed in domain DS2 (blasts B7 to B12, point markers). A different discrete fracture network is built for each domain.

Figure 9 shows stereo projections of the datasets obtained for both domains. For the in-borehole measurements (Fig. 9, two upper left plots), three sub-vertical high pole density areas (N, SE and SSE sets), and a
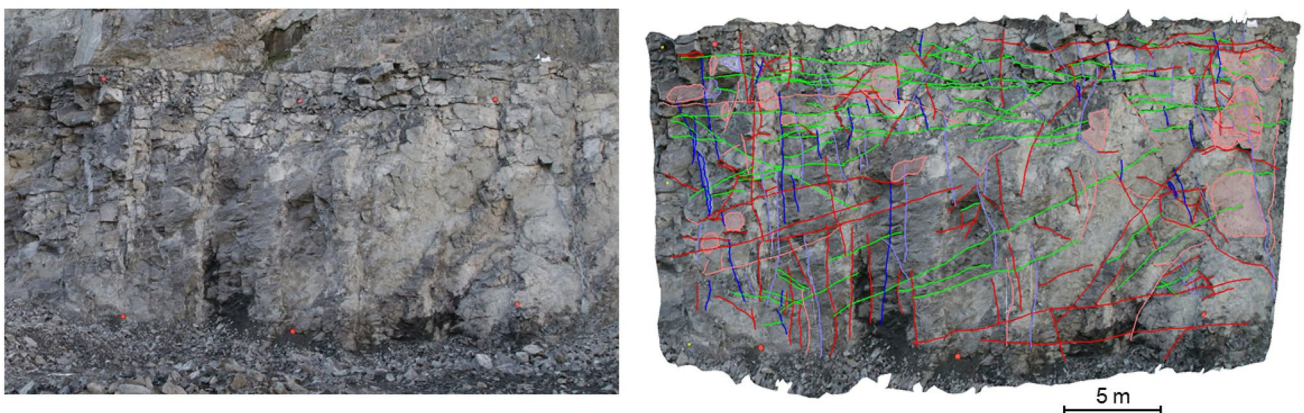

Fig. 4 Left: example of field photo for blast B10; right: photogrammetrically reconstructed 3D model with recognized facture traces and facets (filled polygons)

Table 2 Area covered with photogrammetry restitution and distribution of recognized fracture traces for each blast

Blasts	B1	B2	B3	B4	B5	B6	B7	B8	B9	B10	B11	B12
Surface area of highwall, m²	390.4	388.3	316.1	247.9	303.3	264.3	371.8	410.1	343.6	431.3	376.1	308.3
Highwall face pole orientation, °/°	50.1/73.4	54.9/67.7	50.6/71.6	45.7/71.9	42.6/72.2	45.5/73.1	40.6/68.7	49.9/81.2	42.3/65.8	49.6/77.9	43.1/69.4	41.7/72.2
No. of identified traces	86	55	51	91	59	77	141	165	267	202	206	242
Total trace length, m	250.6	180.3	194.4	235.8	170.5	180.4	326.6	333.5	605.1	510.5	463.6	301

sub-horizontal one are apparent in both DS1 and DS2. The SE and SSE-dipping sub-vertical sets are merged in the density plot of DS2 due to the high total number of poles. The photogrammetry data (Fig. 9, two lower left plots) show the four areas of high pole density seen in the televiewer measurements plus an SvSW set, barely apparent in the televiewer plots. This set corresponds to fractures that are nearly parallel to the free face for which only the facets are considered, while traces have been discarded as their orientation measurement is prone to large errors. Both DS1 and DS2 plots present a blind area towards N for medium to large dip angles, because such fracture planes have a similar direction as the face: this causes a weak presence of the SvN set in the highwall faces. The outcrops data (Fig. 9, right plot) clearly present a sub-horizontal set and three sub-vertical sets, including an East–West dipping one, which is associated with the SvSW set and somewhat compensates this sampling bias on the highwall. Regional tectonic events can be recognized in the resulting discontinuity clusters from all televiewer probe monitoring, photogrammetry scan and external outcrop samplings. This justifies the tectonic genesis of the observed families and has been used to guide the sectorization to fit parametric models of orientation distribution functions in each family.

The Terzaghi correction (Terzaghi 1965) was tested for the different sets according to their orientations with respect to the sampling direction. However, the maximum correction factor turned out to be relatively small (around 20% at most), being of the same order as the natural measurement error. In these conditions, as explained by Wang and Mauldon (2006), errors proportional to the correction may be introduced into the data, risking an actual worsening of the quality of the data as measured. For this reason, the correction was not applied.

3 Discrete Fracture Network Models and In Situ Block Size Distributions

The basic workflow to produce the DFN model can be summarized in four steps: (i) the identification of fracture orientation sets through the analysis of stereoplots; the parameters for the fracture set spherical probability models (mean pole vector and concentration parameters) are initially estimated from manual sectoring, used as initial condition for the computational family clustering; (ii) the identification of potential models for fracture size from bench wall surface fracture trace length data; (iii) the choice of a description of the spatial positioning of fractures (in terms of their centroids) through an assessment of the random versus clustered arrangement of discontinuities; (iv) the adjustment of the fracture number
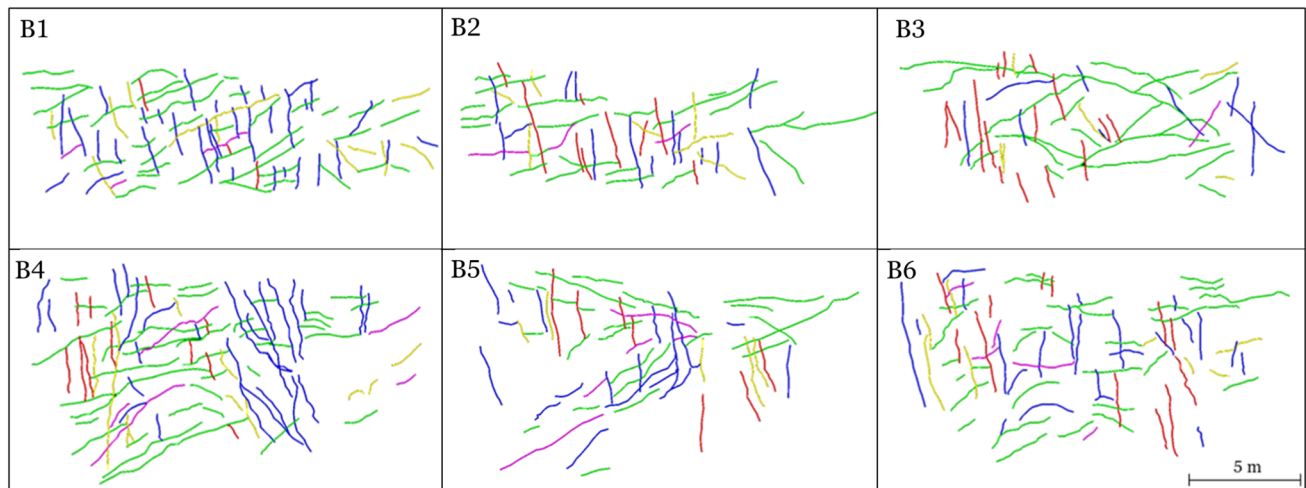
Fig. 5 Tracemaps of bench faces 1–6 (DS1): Sh green, SvSSE yellow, SvSE blue, SvN red, SvSW magenta (see Sect. 2.3 for the description of the sets of discontinuities) (Color figure online)
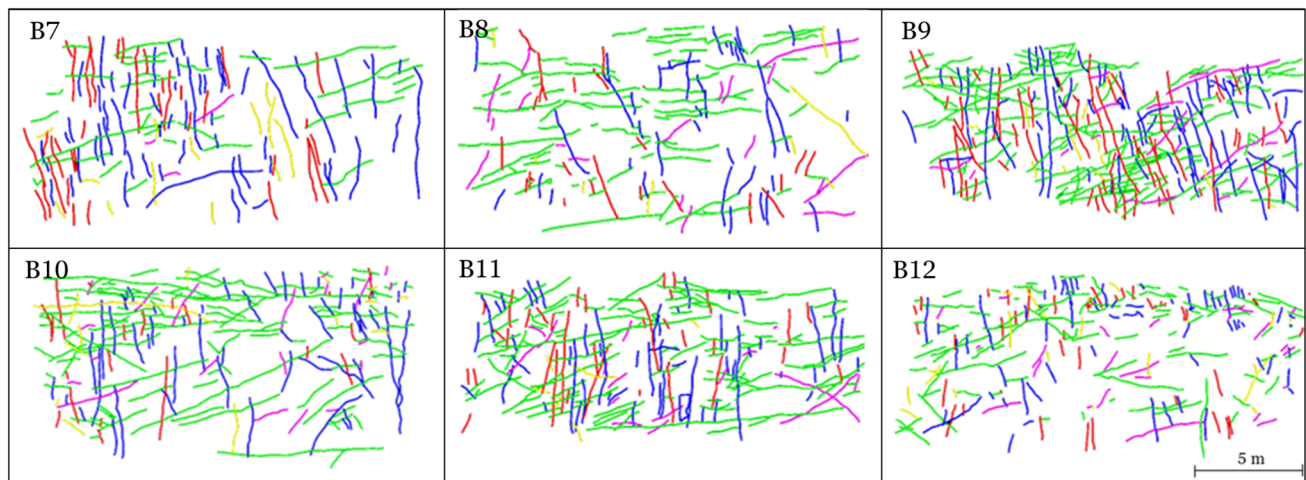

Fig. 6 Tracemaps of bench faces 7 to 12 (DS2): Sh green, SvSSE yellow, SvSE blue, SvN red, SvSW magenta (see Sect. 2.3 for the description of the sets of discontinuities) (Color figure online)

on measured linear and areal fracture densities (P_{10} and P_{21}, respectively, shown in the abscissas of Fig. 10). The whole process was done with FracMan® software. As a stochastic model, the DFN is built on a set of parametric statistical distributions which must be estimated with enough degree of confidence. Despite the large amount of data used here, which gives robustness to the estimates of these functions, a number of assumptions must be made when creating the model. For example, the fractures are modelled as flat discs in space, while they should present irregular and warped surfaces to ideally represent the rock mass. As the number of available models to simulate the spatial distribution pattern of the fractures is limited (Baecher, Levy-Lee, Poisson, density based), the amount

of data has only allowed to define the model on stochastic point processes, rather than density based. The latter is perhaps a more desirable spatial model, considering the importance of the P_{32} fracture density and the wide range of fracture sizes. However, it is not of great interest for the purpose of IBSD building in a context of rock blasting, as the fine end of the IBSD is not as interesting as the coarse part since fines are abundantly created from the extremely high stresses created by the blast, and are less dependent on the IBSD fine end. This is revisited in Sect. 4.

The model regions ('region boxes') considered for the stochastic simulation of the DFN model are $28 \times 28 \times 14$ m for DS1 and $16 \times 51 \times 14$ m for DS2. The planimetric dimensions are selected so that the plan surface is similar

Fig. 7 Examples of CFI plots from different borehole televiewer logs. First campaign data (DS1) in red and second campaign (DS2) in blue (Color figure online)
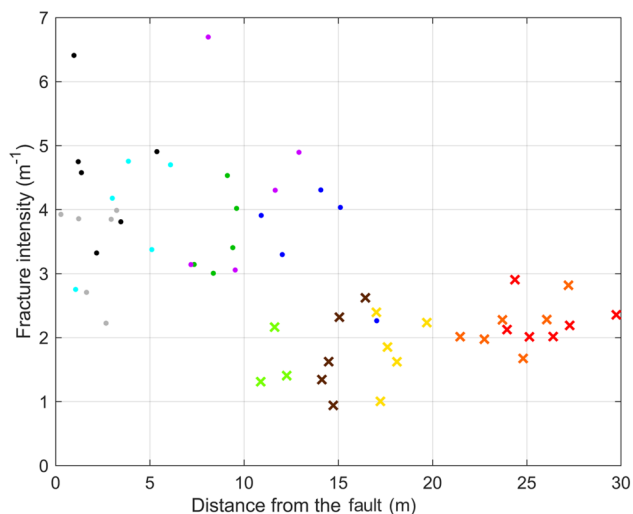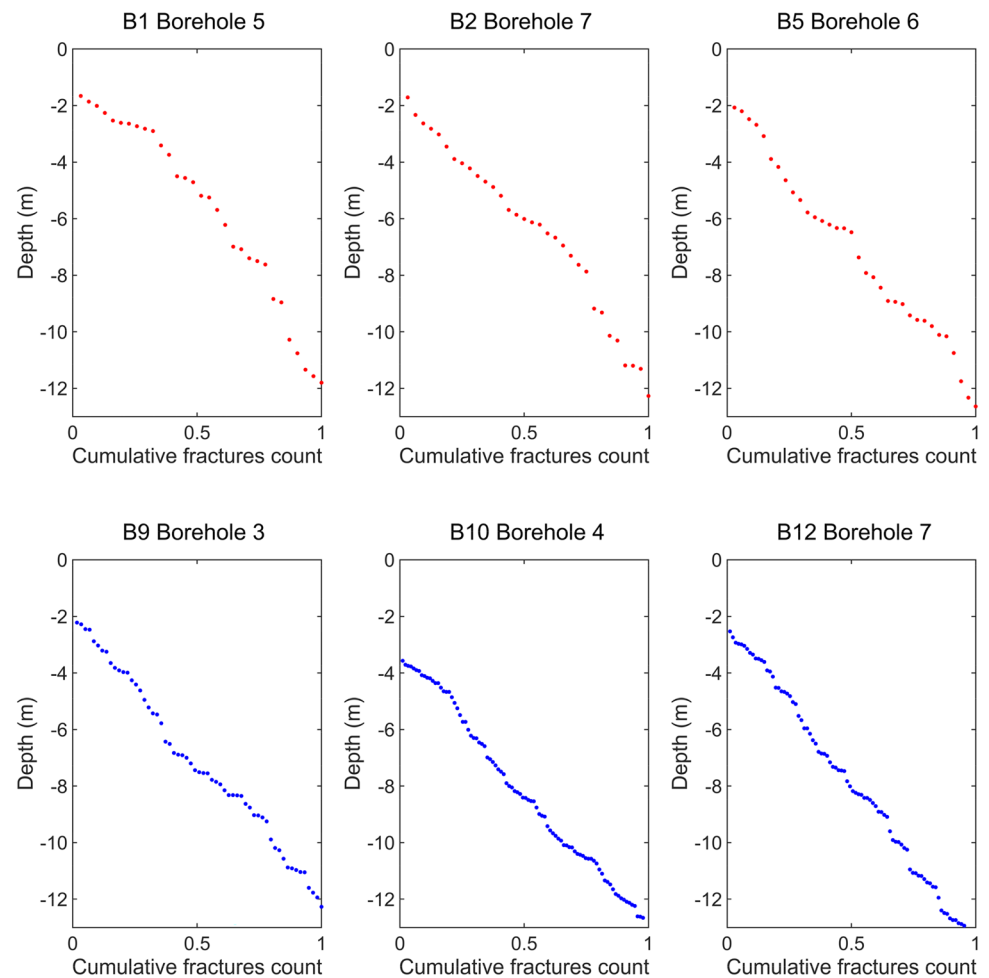

Fig. 8 Fracture intensity with respect to the distance from the fault. Cross markers: DS1; dot markers: DS2

to the areas of the blocks in each domain (Fig. 1). Separate DFN models are built on each domain for each fracture set, calibrating P_{32} (using the total number of fractures in the region box as variable) with P_{10} and P_{21} as target values (Miyoshi et al. 2018) for each family. The best fit of the experimental distributions of trace length are provided by lognormal distributions of fracture size. Fracture centre points are distributed in space according to the Baecher model (Baecher et al. 1977) in each of the spatial domains DS1 and DS2. Each set is generated repeatedly in FracMan® with different numbers of fractures until the resulting mean densities P_{10} and P_{21}, at the boreholes or highwall faces, respectively, are equal to the observed ones within a tolerance of 3%. The DFN model used is supported by the statistics of the distributions used for the orientations, fracture sizes and spatial location of each family, which would allow the generation of an infinite number of statistically similar models adjusted to the P_{21} and P_{10} of the highwall faces and televiewers, respectively. No attempt has been made to carry out a sensitivity analysis, or to find the impact of the DFN variability on the IBSD.
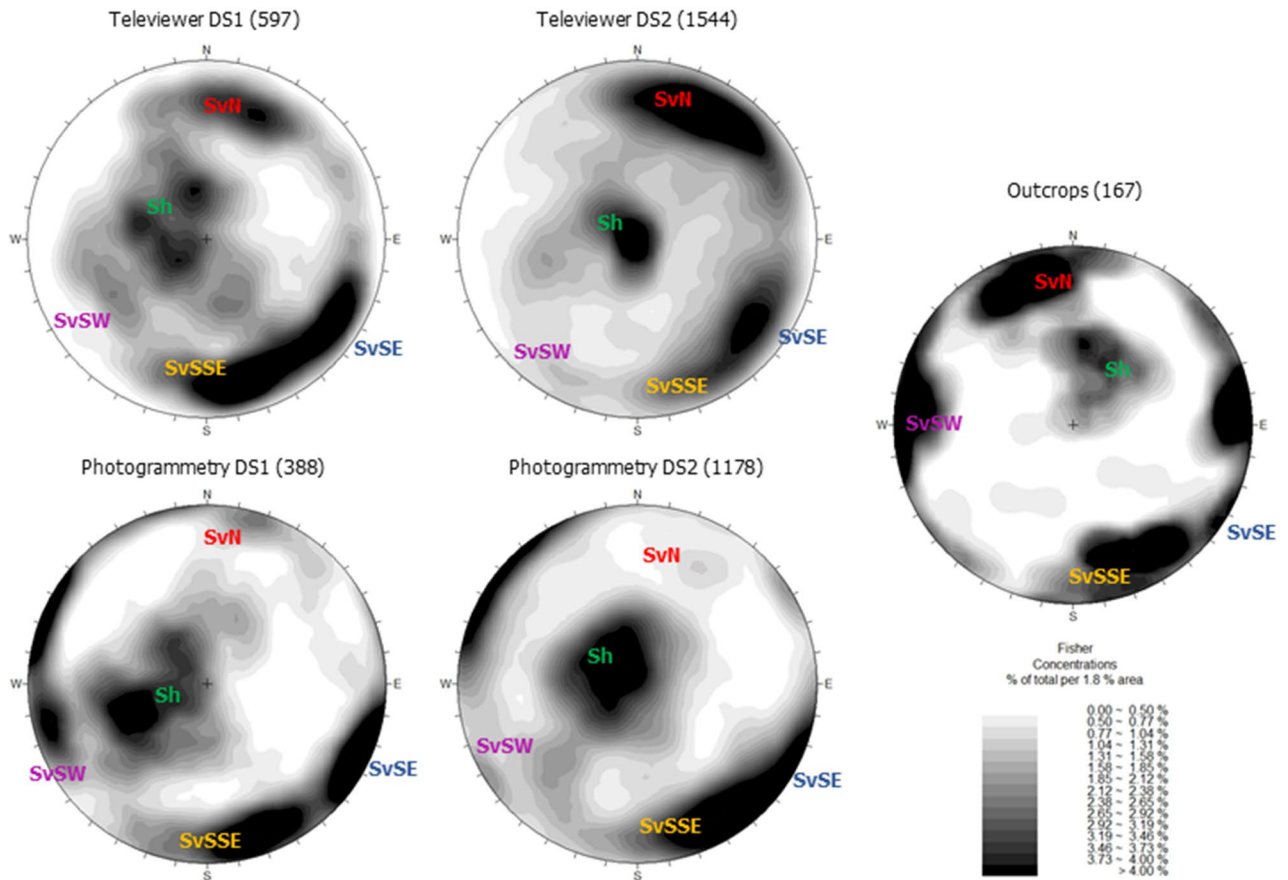
Fig. 9 Stereographic representation of poles of fractures observed in televiewer, photogrammetry, and outcrops data for both domains DS1 and DS2
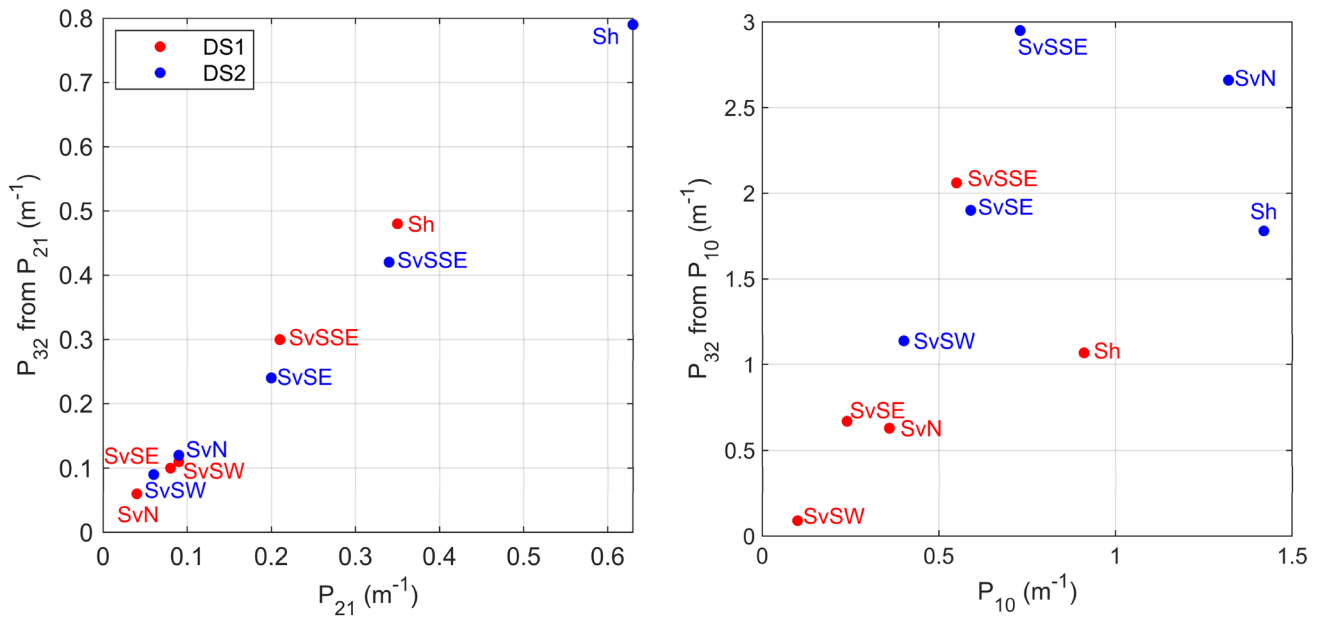

Fig. 10 Calibrated density parameter P_{32} versus measured P_{21} (left) and P_{10} (right)

Table 3 Calibrated number of fractures from P_{21} and P_{10} (DS1–DS2; volumes of both region boxes are similar so that the number of fractures can be compared) and the resulting P_{32} densities in m^{-1} from both calibrations

Set	N_{P21}	N_{P10}	N_{P10}/N_{P21}	P_{32} from P_{21}	P_{32} from P_{10}
Sh	676–2355	1558–5070	2.3–2.2	0.48–0.79	1.07–1.78
SvSW	251–239	920–11,642	3.7–48.7	0.10–0.09	0.09–1.14
SvSSE	446–1807	3038–12,223	6.8–6.8	0.30–0.42	2.06–2.95
SvSE	205–1101	1176–8355	5.7–7.6	0.11–0.24	0.67–1.90
SvN	75–601	883–12,666	11.8–21.1	0.06–0.12	0.63–2.66

The number of simulated discontinuities required to match P_{21} and P_{10} is significantly different (Table 3), with the number of fractures from P_{10} calibration being higher. The ratio between the number of fractures from P_{10} and P_{21} is also given in Table 3: this varies from 2.3 (Sh) to 11.8 (SvN) for DS1 and from 2.2 (Sh) to 48.7 (SvSW) for DS2. Table 3 also gives the resulting P_{32} densities. By way of assessment of the fracture intensities, P_{21} and P_{10} are plotted versus P_{32} in Fig. 10; both relations are neatly monotonic, although the latter shows a larger scatter. The information on spacing and orientations from the borehole survey (a mere fracture count along a line) is not enough to replicate the three-dimensional complexity of the fracture network. To reduce the scattering of the linear relation between P_{32} and P_{10} intensities (Fig. 10—right), the number of sampled
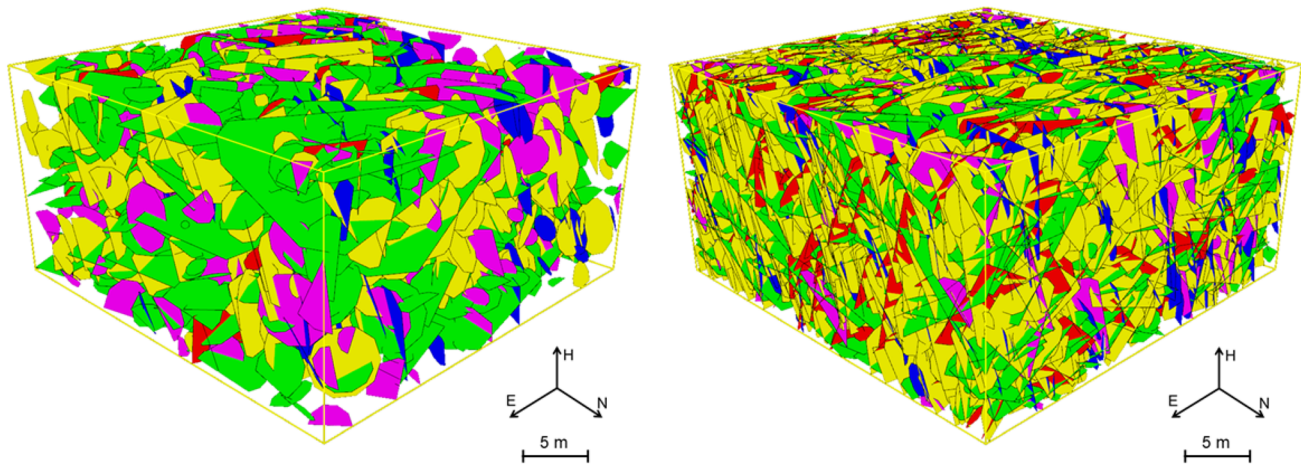

Fig. 11 Composed DFN model for DS1 at the highwall (left) and borehole (right) scales. Sh green, SvSSE yellow, SvSE blue, SvN red, SvSW magenta (Color figure online)
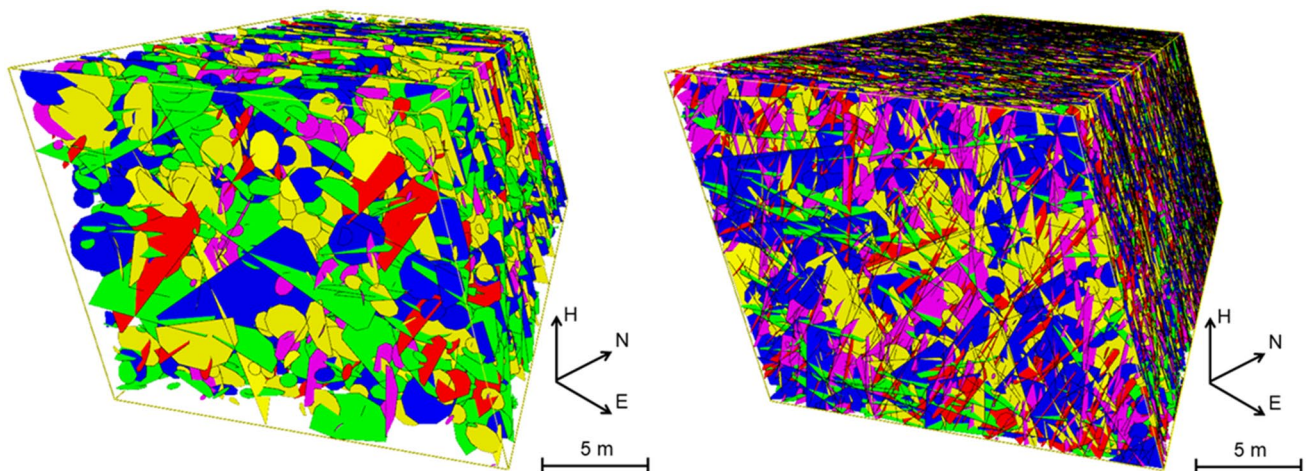

Fig. 12 Composed DFN model for DS2 at the highwall (left) and borehole (right) scales. Sh green, SvSSE yellow, SvSE blue, SvN red, SvSW magenta (Color figure online)
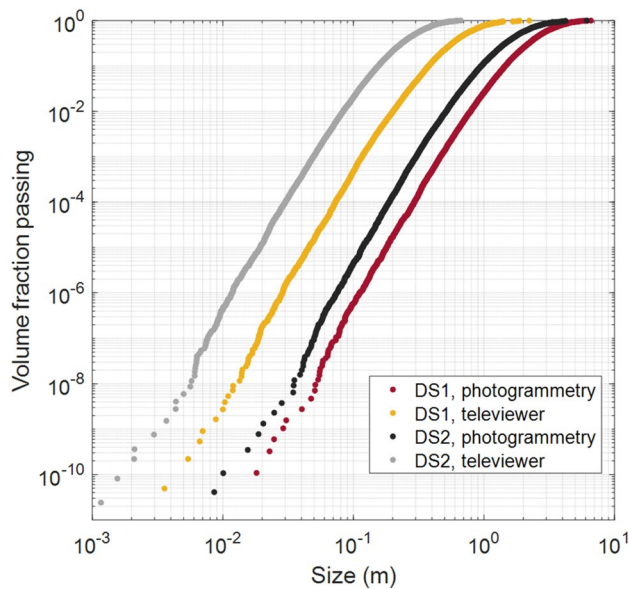
Fig. 13 In situ block size distributions for the models calibrated on P_{21} (photogrammetry) and P_{10} (borehole) for DS1 and DS2

boreholes should be ideally much larger than that measured in this study, so that the P_{10} estimation is more robust for each discontinuity set in the whole rock mass. Besides, fracture lengths provided by photogrammetry improve the proportionality of P_{32} versus P_{21}, reducing the scattering of this relation (Fig. 10—left).

Once the numbers of fractures in each family and domain are obtained (Table 3), the complete DFN models in the DS1 (Fig. 11) and DS2 (Fig. 12) domains are obtained at both the highwall (left plots) and borehole (right plots) scales.

The multi-dimensional spacing (MDS) calculation method in FracMan® is chosen to obtain the synthetic IBSD (Dershowitz et al. 1998) from the DFNs. This algorithm selects random points in a defined domain and generates a series of scanlines in three orthogonal directions (N, E and H axes) from them. This could lead to unrealistic shapes of the blocks due to the independency of the spacing sampled in different directions, but this should not affect the estimation of volumes, and their equivalent size defined as the edge of a cube of equal volume. Other available algorithms have also been tested but they do not fit properly to the configuration of the study case and the characteristics of the fracture sets. The number of randomly selected points for the four models varies from 600,000 to 4,000,000. Those numbers are chosen so that sampling is performed down to the finer blocks (i.e. the sampling distance is in the range of the smaller discontinuity spacing). The boundaries of the region box where the sets are simulated are considered as fractures censoring the block size limited by the face. To obtain a significant sample of the block size population, a total of 10,000 samples are drawn. The resulting cumulative volumetric distributions of

block sizes (fraction of rock volume in blocks of sizes less than the variable) are shown in Fig. 13 for each domain and measuring method. Note that the distribution is expressed here in the common way used for cumulative fragment size distributions, i.e. volume fraction (mass fraction is used for fragments) of blocks of size less than the variable (size, and not volume, is used as variable, unlike common representations of IBSD); see also Gama 1983.

4 Discussion

The four IBSDs show different results in terms of sizes, larger for the models calibrated on P_{21} than those calibrated on P_{10}, consistent with the higher density of fractures in the televiewer logs than in the photogrammetry surveys. Likewise, the size distributions of DS2 are finer than DS1 as the fracture density is higher in the former. Note the close collinearity of the distributions, stemming from the similar orientations of fractures in both domains, and with both measurement techniques.

Gamma, Rosin–Rammler–Weibull (RRW) (Rosin and Rammler 1933; Weibull 1939, 1951) and Gates–Gaudin–Schuhmann (GGS, a power law, Schuhmann 1940, 1960) functions were fitted to the cumulative block size distributions:

$$\text{Gamma}: F(x) = Pr(X < x) = \frac{1}{b^n \Gamma(n)} \int_0^x t^{n-1} \exp(-t/b) \mathrm{d}t, \tag{1}$$

b and n being the scale and shape parameters, respectively. Γ is the Gamma function.

$$\text{RRW}: F(x) = Pr(X < x) = 1 - \exp\left[-\ln 2\left(\frac{x}{x_{50}}\right)^n\right], \tag{2}$$

x_{50} and n being the scale (median) and shape parameters, respectively.

$$\text{GGS}: F(x) = Pr(X < x) = (x/x_{\max})^n, \tag{3}$$

$x_{\max}$ and n being the scale and shape parameters (maximum size and log–log slope), respectively.

RRW and GGS have long been used to represent rock fragment size distributions from blasting and from other fragmentation processes such as starting with crushing and grinding (Harris 1968; Koshelev et al. 1971; Lundborg 1971; Larsson 1974), followed by a large number of rock fragmentation-related studies, noticeably the Kuz-Ram model (Cunningham 1983, 1987, 2005), arguably the most widely used rock fragmentation by blasting prediction formulae system that uses the RRW distribution as base formula. GGS and modifications thereof (Gaudin and Meloy 1962; Bergstrom 1966; Harris 1968) in turn are preferred
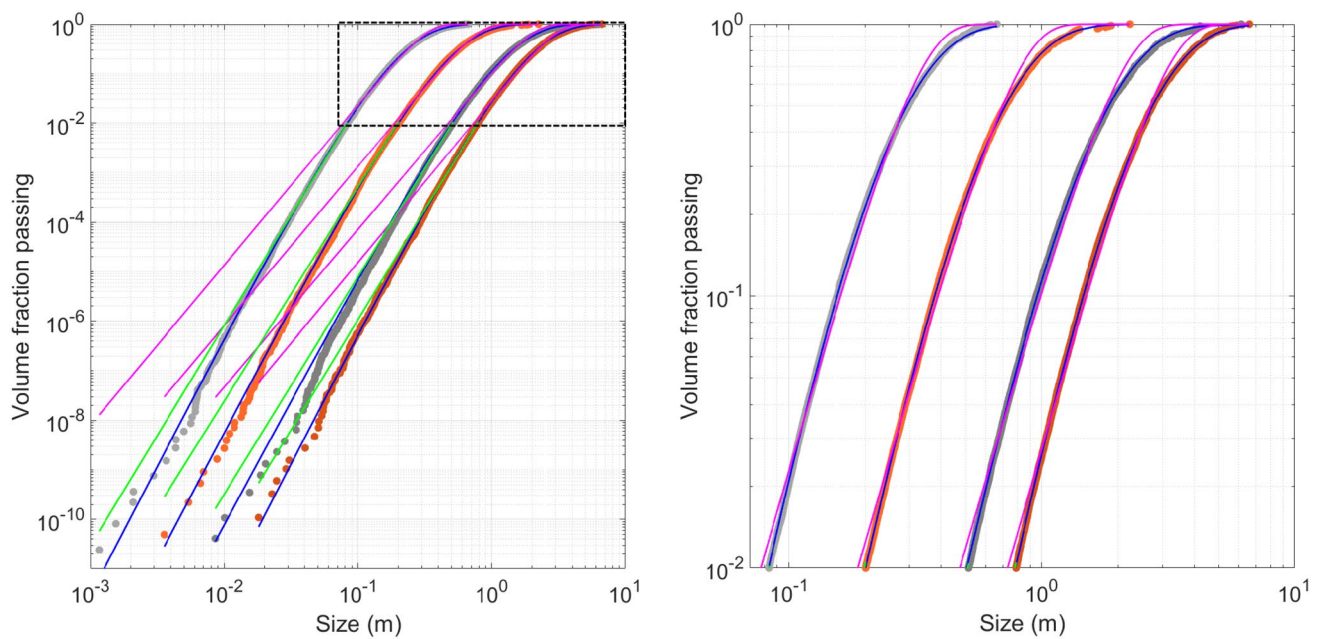
Fig. 14 Distribution function fits to IBSD. Blue: Gamma; magenta: RRW; green: GGS. The right graph shows a zoom on large sizes and the rollover zone

Table 4 Functions fitted to the IBSD

	Shape	Scale, m	MARE[a]	K–S test[b] p value	K–S stat
DS1—P_{21}					
Gamma	5.2859	0.5528	0.0083	0.933	0.024
RRW	3.2583	3.0000	0.1102	7.44E-07	0.121
GGS	4.4446	2.2033	0.0258	0.257	0.045
DS1—P_{10}					
Gamma	5.1555	0.1482	0.0171	0.933	0.024
RRW	3.2149	0.7832	0.1088	3.54E-07	0.124
GGS	4.3230	0.5769	0.0450	0.130	0.052
DS2—P_{21}					
Gamma	5.0273	0.3911	0.0188	0.789	0.029
RRW	3.1804	2.0122	0.1125	2.60E-08	0.134
GGS	4.3903	1.4531	0.0361	0.334	0.042
DS2—P_{10}					
Gamma	5.2229	0.0599	0.0118	0.823	0.028
RRW	3.2317	0.3214	0.1047	9.71E-06	0.110
GGS	4.4468	0.2337	0.0199	0.884	0.026

[a]Median absolute relative error

[b]The critical K–S statistic for the comparisons of the original distributions and the fitted ones is 0.0607 at significance 0.05. The test of the fit is positive (i.e. the hypothesis that samples from the original and from the fitted function come from the same distribution is not rejected) if the K–S statistic is less than the critical.

for crushing and grinding comminution where a maximum size (e.g. the single-particle crusher or mill feed size) can be clearly identified (Harris 1968; Wills 1992); RRW is also largely used in particle comminution, including an upper truncated variety of it (King 2001; Tavares 2004). Contrary to RRW and GGS, the Gamma distribution is rarely used for describing rock fragmentation; an exception is the work by Faramarzi et al. (2015).

The fitted distributions are plotted in Fig. 14. The power law is fitted at fractions passing below 10^{-2} m to determine the slope of the log–log quasi-linear tail of the distributions, as it does not have the upper roll feature of the Gamma or RRW. The parameters and some goodness of fit data are given in Table 4. The performance of the Gamma distribution is outstanding, providing an excellent fit across the whole size-passing range, with a median absolute relative error (MARE, see Table 4) less than 2% in all cases, and with high p values in the K–S test and low K–S statistic. This result perhaps stems from the Poisson process nature of the Baecher's model fracture generation (Cowan et al. 2003). Conversely, the RRW does not provide a good fit in the upper or in the lower sections of the distribution, other than perhaps in the range $0.01 < P < 0.5$; large errors and high K–S statistics rule out this function for representing the IBSD over the whole range in the present case. Reflecting the parallelism of the distributions, the shape parameter of the Gamma distributions varies in a tight range, between 5.03 and 5.29, and the same happens for the exponent of the power functions, between 4.32 and 4.45 (and even if the fits are not good at large, the RRW exponents also show a consistent behaviour).
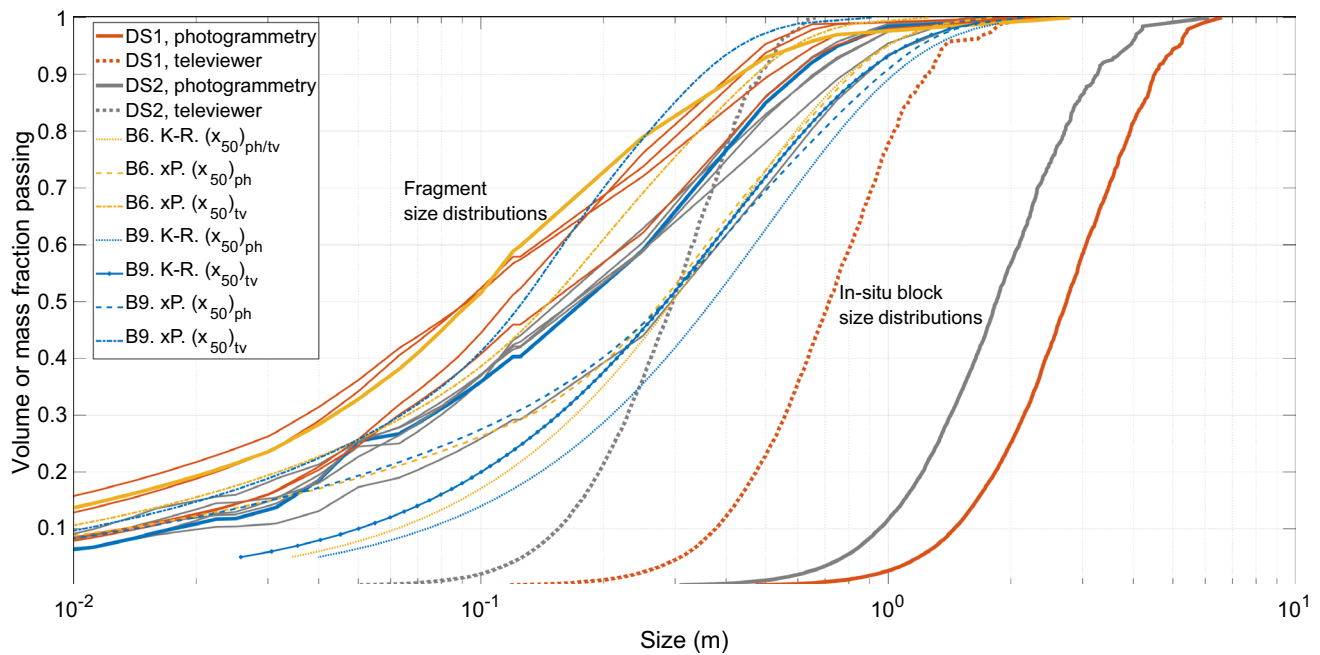
Fig. 15 Fragment size distributions from blasting (thin solid lines; red: DS1, grey: DS2) and IBSD (thick lines, see legend). Fragmentation models' predictions: B6 yellow, B9 blue; dotted and dotted-solid: Kuz-Ram; dashed and dotted-dashed: xP-frag; see legend. Experimental distributions B6 and B9 are highlighted in thick solid yellow (B6) and blue (B9) lines (Color figure online)

The different location of the IBSD from the two field sampling methods stems from the different number and spacing of fractures measured; this difference is explained by two main factors. (i) The photogrammetry analysis has a lower resolution in terms of GSD that was 8.5 mm for the photogrammetry and 1 mm for the televiewer. The lower limits of fracture trace length mapped from photogrammetry models are about 0.5–1 m for DS1 and 0.1–0.5 m for DS2. Thus, not all outcropping discontinuities are distinguishable and can be marked by the operator. (ii) The televiewer analysis works on a smaller scale and allows the operator to detect tiny features of the rock, even those that may not likely open upon blasting (e.g. lineation and veins) and that should hardly be considered sides of blocks.

Despite the different locations of the four IBSD, covering different size ranges, the constant log–log slopes of the tails provide evidence of multi-scale validity and a scaling invariant structure (more than two orders of magnitude) of discontinuities of the rock mass. The similar shape factor values of the Gamma distributions show that the invariant structure is preserved along the sampling range.

The fragment size distributions of the blasts carried out in each of the twelve bocks characterized were determined by on-site sieving with a mobile screen; the procedure is described and the fragmentation measured is presented in detail and discussed against blast design in a companion paper (Sanchidrián et al. 2022). The fragment size distributions are shown in Fig. 15 (eleven curves are plotted; for one

blast, the coarse cut measurement could not be made so its results were not used), together with the IBSDs for the different domains, from televiewer and photogrammetry measurements; a semi-log plot is used, a common representation of IBSD and also of blasting fragment size distributions, see e.g. Latham et al. (2006) and Bamford et al. (2020). The shock waves radiating from the blastholes, and the high-pressure gases, initially in the range of GPa, crush the rock in the vicinity of the holes and open new shear cracks. Cracks propagate, branch and merge, creating new fragments much smaller than the initial blocks in the rock mass. The large generation of fine material results in cumulative size distributions as those shown in Fig. 15 (log–log slopes around or less than 1 are common). The effect of the blast is (i) to shift the size distribution to the left—towards smaller sizes—and (ii) to incorporate a large amount of fine and very fine material, reducing the overall slope of the distribution. In statistical terms, a reduction of the location parameter and an increase of the variance occur. Note the inconsistent location of the televiewer's IBSD in DS2 that overlaps the size distributions of the fragmented rock, i.e. the coarser sizes are smaller than the larger blocks observed after blasting. This does not happen—or does to a very minor extent—for the televiewer's IBSD of DS1, in which the maximum size is similar to the maximum blasted sizes. Televiewer logs record even tiny features of the rock, resulting in overall smaller sizes in the block construction. This feature does not favour televiewer as source of data for building the IBSD,

though televiewer data has proved to be helpful in the identification of the fracture domains and the definition of the orientation sets; however, televiewer data are not sufficient for an estimation of the fracture length (hence the large scatter of the P_{32} vs P_{10} relation; see Fig. 10). Photogrammetry data does provide this information from the fracture maps of the highwall surface, making photogrammetry surveying essential for a description of the fractures.

The median in situ block size is commonly used as an equivalent to the mean principal joint spacing (see e.g. Latham and Lu 1999), particularly convenient when there are several joint sets. Their impact on the predictions by blast fragmentation models has been tested with the Kuz-Ram (Cunningham 1983, 1987, 2005) and xP-frag (Sanchidrián and Ouchterlony 2017) models. The rock and blasting data employed in the calculation are given in Sanchidrián et al. (2022). The results are plotted in Fig. 15 as examples for two blasts: B6 (first campaign, DS1) and B9 (second campaign, DS2). For each blast, the two IBSD medians were used: for DS1, 2.74 m and 0.72 m for photogrammetry and televiewer, respectively; for DS2, 1.84 m and 0.296 m. Note that for the Kuz-Ram model, only one distribution is plotted for blast B6; the prediction is identical to the two medians, as the joint spacing factor is defined at intervals of joints spacing, and the two DS1 IBSD medians fall in the same interval; this does not happen for DS2. The predicted curves lie generally within the bundle of measured distributions, with shapes and slopes comparable to the measured curves, the photogrammetry-derived ones yielding, as expected, coarser fragmentation than the televiewer. xP-frag seems to be more sensitive to the IBSD median and to yield finer fragment size distributions than Kuz-Ram in this case. The prediction with the televiewer IBSD is quite acceptable for B6 (this blast is in DS1 where the televiewer IBSD is, as discussed above, acceptable); for B9 the xP-frag prediction with televiewer results in a distribution with too small sizes particularly in the upper zone, and a strong bending downwards compared with the measured distributions, a possible result of the obviously incongruous position of the televiewer's IBSD in DS2. This consistency test does not purport to be an assessment of the application of the Kuz-Ram or xP-frag models or a discussion of their merit or predictive accuracy. Although this might probably be an interesting exercise, it is beyond the scope of this paper.

5 Conclusions

Discontinuities were monitored in the inner walls of 57 boreholes with optical televiewer and in 3D models of 12 bench faces reconstructed through photogrammetry. Five fracture sets were identified and characterized in terms of spatial distribution, density parameters (P_{10} and P_{21}), and trace length

statistical parametric distributions. Two different fracture domains were defined in terms of fracture density, related to the distance from a major extensional fault, the density of fractures being higher in the zone closer to the fault. In both domains, the density of fractures was consistently higher for the televiewer observations than for the photogrammetry ones.

A DFN model was created for each fracture domain in which distributions of orientation and size were determined for each fracture set. Fractures were generated in space on a Baecher distribution, at a density such that the calculated densities P_{10} and P_{21} matched the borehole and surface measured ones, respectively. Four fracture models were created, two for each of the domains, one from televiewer data and another from photogrammetry data. Intensity parameters were verified through their mutual relationships (Fig. 10). The multi-dimensional spacing (MDS) algorithm (Dershowitz et al. 1998) was adopted to sample the population of simulated blocks from the calibrated DFN models to calculate the IBSD. The FracMan® software suite was used in this process.

Gamma, Rosin–Rammler–Weibull (RRW) and the power law Gates–Gaudin–Schuhmann (GGS) distributions were tested to represent the IBSD obtained. The performance of the Gamma distribution is found to be outstanding, while the RRW performs poorly. The GGS, fitted only to the fines range (less than 10^{-2} m fraction passing), shows a good fidelity. The Gamma distribution has been frequently applied to describe discontinuity spacings (Huang and Angelier 1989; Gross 1993; Bonnet et al. 2001; Stavropoulou 2014; Tan et al. 2014; Massiot et al. 2015; Bamford et al. 2017), but not, to the authors knowledge, to describe IBSD. Conversely, a number of previous studies, e.g. Lu (1997), consider RRW, together with GGS and log-linear equations to describe simulation results of the IBSD. Aler et al. (1996) also used RRW distribution to fit the IBSD.

The four IBSD (one from each discrete fracture network built) involve different locations, covering different size ranges, those deriving from higher density of fractures yielding smaller block sizes. The constant log–log slopes of the tails provide evidence of multi-scale validity and a scaling invariant structure (more than two orders of magnitude) of discontinuities of the rock mass. Besides, the similar shape factor values of the Gamma distributions imply that the invariant structure is preserved along the sampling range.

The photogrammetry sampling scale involves that not all outcropping discontinuities are distinguishable, so they cannot be marked by the operator. For its part, televiewer logs sampling tends to record even tiny features of the rock, resulting in overall smaller block sizes in the DFN to the point, in one case, that the maximum sizes of the IBSD from televiewer are significantly smaller than the larger fragments observed after blasting. This indicates that some of the

discontinuities observed in the televiewer logs are not activated by the blast either because they are too small, or too tight, or just not even joints but other planar features such as banding, foliation, etc. These features, common in stress metamorphic rocks as the mylonite in this work, do not represent discontinuities or weakness surfaces. This probably rules out the IBSDs determined at the televiewer's borehole scale unless very expert judgement is exercised to censor non-jointing planar features. Conversely, IBSDs from photogrammetry traces were capable of consistently replicating the scaling characteristics for smaller block sizes obtained from borehole DFN models, providing a lower dispersion in the P_{32} versus P_{21} scatter plot. This makes photogrammetry a more complete, standalone surveying technique. It is also faster and easier to apply than the televiewer logging. If photogrammetric models are dense enough, automatic or software-assisted joint detection algorithms could contribute to the acquisition of a proper and inexpensive fracture description of the rock, upon which an in situ block size distribution can be built.

References

3GSM (2010a) ShapeMetriX 3D®; Version 4.4.2

3GSM (2010b) BlastMetriX 3D®; Version 4.4.3

Advanced Logic Technology (2017) WellCAD® software 5.1, Version TK160126

Aler J, Du Mouza J, Arnould M (1996) Measurement of the fragmentation efficiency of rock mass blasting and its mining applications. Int J Rock Mech Min Sci Geomech 33:125–139. https://doi.org/10.1016/0148-9062(95)00054-2

Baecher GB, Lanney NA, Einstein HH (1977) Statistical description of rock properties and sampling. 18th US Symp Rock Mech USRMS 1977 1–8

Bamford T, Esmaeili K, Schoellig A (2017) A real-time analysis of rock fragmentation using UAV technology. Int J Min Reclam Environ 31:439–456. https://doi.org/10.1080/17480930.2017.1339170

Bamford T, Medinac F, Esmaeili K (2020) Continuous monitoring and improvement of the blasting process in open pit mines using unmanned aerial vehicle techniques. Remote Sens 12(17):2801. https://doi.org/10.3390/rs12172801

Bergstrom BH (1966) Empirical modification of the Gaudin-Meloy equation. AIME Trans 235:45

Boersma Q, Athmer W, Haege M et al (2020) Natural fault and fracture network characterization for the southern Ekofisk field: a case study integrating seismic attribute analysis with image log interpretation. J Struct Geol 141:104197. https://doi.org/10.1016/j.jsg.2020.104197

Bonnet E, Bour O, Odling NE et al (2001) Scaling of fracture systems in geological media. Rev Geophys 39:347–383. https://doi.org/10.1029/1999RG000074

Brown ET (2002) Block caving geomechanics. Jul Kruttschnitt Miner Res Centre Brisbane Univ Queensl Press

Brzovic A, Rogers S, Webb G et al (2015) Discrete fracture network modelling to quantify rock mass pre-conditioning at the El Teniente Mine, Chile. Trans Inst Min Metall Sect A Min Technol 124:163–177. https://doi.org/10.1179/1743286315Y.0000000019

Cowan R, Quine M, Zuyev S (2003) Decomposition of Gamma-distributed domains constructed from Poisson point processes. Adv Appl Probab 35:56–69

Cunningham CVB (1983) The Kuz-Ram model for prediction of fragmentation from blasting. In: Proceedings of the 1st international symposium on rock fragmentation by blasting. Sweden: Luleå University of Technology. pp 439–453

Cunningham CVB (1987) Fragmentation estimations and the Kuz-Ram model—four years on. In: Proceedings of the 2nd international symposium on rock fragmentation by blasting. pp 475–487

Cunningham CVB (2005) The Kuz-Ram fragmentation model e 20 years on. In: Proceedings of the 3rd European Federation of Explosives Engineers (EFEE) World Conference on Explosives and Blasting. pp 201–210

Da Gama D (1983) Use of comminution theory to predict fragmentation of jointed rock mass subjected to blasting. In: Rustan A, Holmberg R (eds) Proceedings of 1st International conference on rock fragmentation by blasting, Fragblast 1. Lulea University of Technology, pp 563–579

Dershowitz WS, Einstein HH (1988) Characterizing rock joint geometry with joint system models. Rock Mech Rock Eng 21:21–51. https://doi.org/10.1007/BF01019674

Dershowitz WS, Lee G, Geier J et al (1998) FracMan. Interactive discrete feature data analysis, geometric modelling and exploration simulation. User documentation, version 2.6. Golder Associates, Inc. Redmond, Washington

Dershowitz W, Pointe P La, Doe T (2004) Advances in discrete fracture network modeling. … US EPA/NGWA Fract … 882–894

Elmo D, Yang B, Stead D, Rogers S (2021) A Discrete Fracture Network Approach to Rock Mass Classification. In: International Conference of the International Association for Computer Methods and Advances in Geomechanics. pp 854–861

Elmouttie MK, Poropat GV (2012) A method to estimate in situ block size distribution. Rock Mech Rock Eng 45:401–407. https://doi.org/10.1007/s00603-011-0175-0

Enrile JLH (1991) Extensional tectonics of the Toledo ductile-brittle shear zone, Central Iberian Massif. Tectonophysics 191:311–324

Faramarzi F, Farsangi MAE, Mansouri H (2015) Prediction of rock fragmentation using a gamma-based blast fragmentation distribution model. In: Spathis AT et al. (eds) Proc. 11th International Symposium on Rock Fragmentation by Blasting

(FRAGBLAST11), Sydney, Australia. Carlton Victoria: The Australasian Institute of Mining and Metallurgy, pp 685–692

Gaudin AM, Meloy TP (1962) Model and a comminution distribution equation for single fracture. Trans SME-AIME 223:40–43

Golder Associates Inc (2018) FracMan7-interactive discrete feature data analysis, geomtric modeling and exploration simulation, user documentation, version 7.7. Golder Assoc Inc Redmond

Gross MR (1993) The origin and spacing of cross joints: examples from the Monterey Formation, Santa Barbara Coastline, California. J Struct Geol 15:737–751. https://doi.org/10.1016/0191-8141(93)90059-J

Harris CC (1968) The application of size distribution equation to multi-event comminution processes. Trans SME/AIME 241:343–358

Huang Q, Angelier J (1989) Fracture spacing and its relation to bed thickness. Geol Mag 126:355–362. https://doi.org/10.1017/S0016756800006555

Junkin WR, Ben-Awuah E, Fava L (2019) Incorporating DFN analysis in rock engineering systems blast fragmentation models. 53rd US Rock Mech Symp

Kaiser PK, Amann F, Bewick RP (2015) Overcoming challenges of rock mass characterization for underground construction in deep mines. 13th ISRM Int Congr Rock Mech Int Soc Rock Mech

Kattenhorn SA, Pollard DD (2001) Integrating 3-D seismic data, field analogs, and mechanical models in the analysis of segmented normal faults in the Wytch Farm oil field, southern England, United Kingdom. Am Assoc Pet Geol Bull. https://doi.org/10.1306/8626CA91-173B-11D7-8645000102C1865D

King RP (2001) Modeling and simulation of mineral processing systems. Butterworth-Heinemann

Koshelev EA, Kuznetsov VM, Sofronov ST, Chernikov AG (1971) Statistics of the fragments forming with the destruction of solids by explosion. J Appl Mech Tech Phys 12(2):244–256

Larsson B (1974) Blasting of low and high benches, fragmentation from production blasting. Proceedings of the annual meeting of Swedish rock blasting committee. pp 247–271

Latham JP, Lu P (1999) Development of an assessment system for the blastability of rock masses. Int J Rock Mech Min Sci 36:41–55. https://doi.org/10.1016/S0148-9062(98)00175-2

Latham JP, Van Meulen J, Dupray S (2006) Prediction of in-situ block size distributions with reference to armourstone for breakwaters. Eng Geol 86:18–36. https://doi.org/10.1016/j.enggeo.2006.04.001

Lu P (1997) The characterisation and analysis of in-situ and blasted block size distribution and the blastability of rock masses. A thesis Submitt degree Dr Philos Univ London 169

Lundborg N (1971) Computer program for charge calculations in bench blasting. Technical report DS 1971:18. Stockholm, Sweden: Swedish Detonic Research Foundation

Massiot C, McNamara DD, Nicol A, Townend J (2015) Fracture Width and Spacing Distributions from Borehole Televiewer Logs and Cores in the Rotokawa Geothermal Field, New Zealand. In: Proc World Geotherm Congr 2015 Melbourne, Aust 19–25 April 2015 1–12. https://doi.org/10.13140/RG.2.1.3925.6561

Medinac F, Bamford T, Esmaieli K, Schoellig AP (2018) Pre- and post-blast rock block size analysis using UAV-based data and discrete fracture network. In: 2nd Int Discret Fract Netw Eng Conf DFNE 2018

Miyoshi T, Elmo D, Rogers S (2018) Influence of data analysis when exploiting DFN model representation in the application of rock mass classification systems. J Rock Mech Geotech Eng 10:1046–1062. https://doi.org/10.1016/j.jrmge.2018.08.003

Priest SD (1983) Discontinuity analysis for rock engineering. Chapman & Hall, London, p 473

Riquelme AJ, Abellán A, Tomás R, Jaboyedoff M (2014) A new approach for semi-automatic rock mass joints recognition from 3D point clouds. Comput Geosci 68:38–52. https://doi.org/10.1016/j.cageo.2014.03.014

Rohrbaugh MB, Dunne WM, Mauldon M (2002) Estimating fracture trace intensity, density, and mean length using circular scan lines and windows. AAPG Bull 86(12):2089–2104

Rosin P, Rammler E (1933) The laws governing the fineness of powdered coal. J Inst Fuel 7:29–36

Sanchidrián JA, Ouchterlony F (2017) A distribution-free description of fragmentation by blasting based on dimensional analysis. Rock Mech Rock Eng 50(4):781–806. https://doi.org/10.1007/s00603-016-1131-9

Sanchidrián JA, Segarra P, Ouchterlony F, Gómez S (2022) The influential role of powder factor vs. delay in full-scale blasting: a perspective through the fragment size-energy fan. Rock Mech Rock Eng. https://doi.org/10.1007/s00603-022-02856-1

Schuhmann J (1940) Principles of conmination, I- size distribution and surface calculations. AIME Tech Pub No. 1189

Schuhmann RJ (1960) Energy input and size distribution in comminution. Trans AIME 217:22–25

Stavropoulou M (2014) Discontinuity frequency and block volume distribution in rock masses. Int J Rock Mech Min Sci 65:62–74. https://doi.org/10.1016/j.ijrmms.2013.11.003

Tan Y, Johnston T, Engelder T (2014) The concept of joint saturation and its application. Am Assoc Pet Geol Bull 98:2347–2364. https://doi.org/10.1306/06231413113

Tavares LM (2004) Optimum routes for particle breakage by impact. Powder Technol 142:81–91

Terzaghi RD (1965) Sources of error in joint surveys. Géotechnique 15:287–304. https://doi.org/10.1680/geot.1965.15.3.287

Wang LG, Yamashita S, Sugimoto F et al (2003) A methodology for predicting the in situ size and shape distribution of rock blocks. Rock Mech Rock Eng 36:121–142. https://doi.org/10.1007/s00603-002-0039-8

Wang X, Mauldon M (2006) Proportional errors of the Terzaghi correction factor. In: Proc 41st US Rock Mech Symp - ARMA's Golden Rocks 2006—50 Years Rock Mech

Weibull W (1939) A statistical theory of the strength of materials. Ingeniörvetenskapsakademiens Handl 151:1–45

Weibull W (1951) A statistical distribution function of wide applicability. J Appl Mech ASME 18:7

White DH (1977) Predicting fragmentation characteristics of a block caving orebody. MSc Univ Arizona

Wills BA (1992) Particle size analysis. Mineral Processing Technology, Pergamon Press, Oxford, England, 5th edition, Ch. 4, pp 181–225

Wu H, Pollard DD (1995) An experimental-study of the relationship between joint spacing and layer thickness. J Struct Geol 17(6):887–905

Zhang Q, Wang X, He L, Tian L (2021) Estimation of fracture orientation distributions from a sampling window based on geometric probabilistic method. Rock Mech Rock Eng 54:3051–3075